

Growth Rate Analysis of Gibbsite Single Crystals Growing from Aqueous Sodium Aluminate Solutions

C. Sweegers, H. Meekes, and W. J. P. van Enckevort*

NSRIM Department of Solid State Chemistry, University of Nijmegen, Toernooiveld 1, 6525 ED Nijmegen, The Netherlands

I. D. K. Hiralal and A. Rijkeboer

Billiton Aluminium B. V., Mariahoeveplein 6, 2591 TV The Hague, The Netherlands

Received January 21, 2003

ABSTRACT: In-situ optical microscopy was used to measure the growth rate of gibbsite single crystals growing from aqueous sodium aluminate solutions. The growth rate was measured for various crystal faces, i.e., {100} and {001} faces in case of twinned hexagons and {110} faces for single crystalline lozenges. A considerable dispersion in crystal growth rate was measured: the growth rates varied from crystal to crystal within the same experiment as well as from experiment to experiment. They also fluctuated in time. The origin of this dispersion in growth rates is discussed. The results of the growth rates measured as a function of the driving force, which were averaged over several crystals, were fitted with growth rate equations for various growth mechanisms. It is shown that the birth and spread-type growth rate equation defined by Nielsen (*J. Cryst. Growth* **1984**, *67*, 289–310) as well as an equation derived in this paper for step nucleation growth at the intersection line of contacting crystallites can be used to describe the growth rates of gibbsite in all crystallographic directions.

Introduction

In the Bayer process, which is industrially used to extract aluminum oxide from bauxite, gibbsite is the mineral recovered from the crystallization of aluminum hydroxide (Al(OH)₃) from aqueous sodium aluminate solutions.²

Gibbsite growth proceeds very slowly, typically 1–2 μm/h, and despite a lot of research the effects of crystallization conditions and impurities are still not well established. Detailed knowledge of the crystallization process is necessary to obtain proper insight and a quantitative description. The possibility of predicting the gibbsite growth behavior under various conditions will be very useful, especially for practical purposes.

From earlier work on gibbsite crystallization using batch crystallizers,^{3–6} general growth rate equations were obtained, which are based on

$$R = k_0 \exp\left(\frac{-E}{RT}\right) S^2 \quad (1)$$

Here, k_0 is a kinetic coefficient, E is the activation energy for 2D nucleation, T is the crystallization temperature, and S is the crystallization driving force. Several definitions have been given for the driving force, S . From the fits of the corresponding expression (1) to experimental growth rates, the growth rate constants k_0 and E were obtained. The exact values of these parameters were strongly dependent on the definition of the driving force used. A proper definition for the driving force for crystallization is, therefore, necessary to obtain a realistic description of the growth rate. This will be the subject of the section after this introduction.

The square dependence of the growth rate on the driving force in eq 1 suggests that gibbsite crystallization is controlled by a screw dislocation growth mechanism as was deduced for many crystals growing at low supersaturation in aqueous systems.^{7,8} In the case of ions, they enter from an adsorption layer consisting primarily of constituent ions in an equivalent (electroneutral) ratio. The growth rate equation of gibbsite crystallization based on eq 1 was not based on actual growth mechanisms, but was the result of semiempirical data fit procedures, and therefore this does not reveal the actual growth mechanism. Still, the relation between the growth rate and driving force according to this equation is generally accepted in the literature.

In batch and bulk experiments, the growth rates can be distorted by nucleation, agglomeration, and attrition. Moreover, the growth behavior of different types of crystals and different crystal faces cannot be studied in such experiments. These problems are avoided in experiments in which individual crystals are followed in time to measure their linear growth rate, i.e., the growth rate in well-defined crystallographic directions. Only a few studies have been reported in which the linear growth rate of individual gibbsite crystals was determined. In 1973, King reported measurements on the growth rate of isolated gibbsite crystals attached to a polyacrylate film on a glass slide in various pure sodium aluminate solutions at 80 °C.⁴ He derived a growth rate equation:

$$R = k_0 \left(\frac{c - c_{eq}}{FC}\right)^2 \quad (2)$$

where c and c_{eq} are the actual and the equilibrium Al(OH)₃ concentration of the solution at the crystallization temperature T , and FC is the free caustic, which is the total amount of sodium hydroxide minus the amount

* Corresponding author. W. J. P. van Enckevort, NSRIM Department of Solid State Chemistry, University of Nijmegen, Toernooiveld 1, 6525 ED Nijmegen, The Netherlands. Phone: +31 (0)24 3653433; fax: +31 (0)24 3653067; e-mail: wvenck@sci.kun.nl.

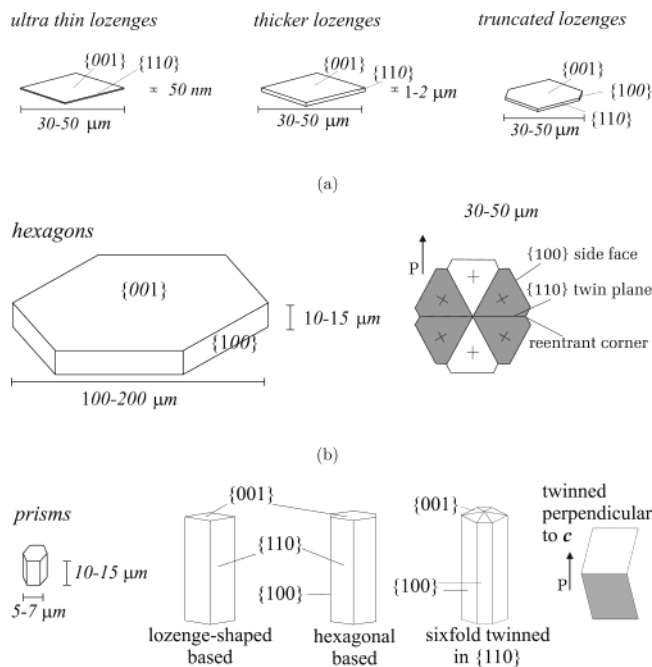


Figure 1. (a–c) Morphologies of different types of gibbsite, γ -Al(OH) $_3$, crystals grown from sodium aluminate solutions under various conditions. For the hexagons, also the top view between crossed polarizers is given, showing 6-fold twinning. The dark areas are in extinction direction for the given polarizer direction, indicated by P. For details, see ref 10.

required to convert aluminum hydroxide to the aluminate ion, Al(OH) $_4^-$.

Lee et al.⁹ carried out an in situ microscopic study on the growth of isolated gibbsite crystals. In this study, the phenomenon of growth rate dispersion was observed. The growth rate was found to vary not only from experiment to experiment, but also from crystal to crystal within the same experiment as well. It was concluded that growth of the prismatic faces occurs via a spiral growth mechanism.⁹ The basal faces grow, above a certain relative supersaturation, by a birth and spread mechanism, while spiral growth is the major mechanism operating below this value of relative supersaturation.

In this study, the linear growth rates of individual faces of different types of gibbsite crystals measured in situ as a function of the driving force are presented. The {001} basal and {100} side faces of 6-fold twinned hexagons, the {110} faces of single crystalline lozenges, and the {001} and side faces of prisms were examined. The indexing of these faces in case of single crystalline and twinned gibbsite crystals has been described in a previous paper.¹⁰ A schematic presentation of the different crystal types is shown in Figure 1. The results will be interpreted using several growth rate equations from the literature in combination with the conclusions derived from surface topographic studies.¹¹ Furthermore, a new model involving multiple contact nucleation at the intersecting line of two contacting crystals is introduced to describe gibbsite crystal growth. In this paper, “contact nucleation” means the 2D nucleation of growth steps on the contact line of a foreign body with the crystal surface. The growth rate equation is derived in the appendix. From this, the relevant growth mech-

Table 1. Definitions for Driving Forces, S , Used in the Literature^a

S	ref
$c - c_{eq}$	3, 5
c/c_{eq}	12, 13
$(c - c_{eq})/c_{eq}$	12, 13
$(c - c_{eq})/C$	2
$(c - c_{eq})/FC$	4
$\sqrt{(c/C - c_{eq}^2/C)/C^{0.5}}$	6

^a c and c_{eq} are the actual aluminum hydroxide concentration and the equilibrium value, respectively, expressed in grams per liter Al $_2$ O $_3$, C is the caustic concentration expressed in grams per liter Na $_2$ CO $_3$, and FC is the free caustic, that is, the total amount of sodium hydroxide minus the amount required to convert aluminum hydroxide to the aluminate ion.

anisms for the individual faces of individual gibbsite crystals are proposed.

Driving Force for Gibbsite Crystallization. In the literature, several definitions are given for the crystallization driving force, S , as used in eq 1. Some authors^{3,5} proposed to use the difference in the actual aluminum hydroxide concentration in the solution and the equilibrium value, i.e., $c - c_{eq}$. Veessler et al.^{12,13} suggested to use the normalized supersaturation ratio c/c_{eq} or $(c - c_{eq})/c_{eq}$ as a measure for the driving force. These expressions should normalize the supersaturation with respect to the solubility of aluminum hydroxide for different caustic concentrations. More attempts to improve the growth rate relation with respect to the driving force led to definitions of the driving force as presented in Table 1. In the last three definitions of this table, the driving force is corrected for the presence of active hydroxide ions, which would result in growth rate relations that are independent of the caustic concentration.^{2,4,6} We will derive an alternative, improved expression for the driving force in this section. The dimensionless driving force for crystallization is defined as $\Delta\mu/kT$, where $\Delta\mu$ is the difference in chemical potential of the growth units in the mother phase and in the solid phase, and kT is the thermal energy. The chemical potential of species i is defined as

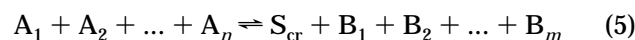
$$\mu_i = \mu_i^\circ + RT \ln a_i \quad (3)$$

where a_i is the activity of the units of species i in the solid or the mother phase. The activity, a_i , is the product of the activity coefficient, γ_i , and the molality of species i , m_i .

For a simple crystallization process, involving one species i and considering that the activity in the solid equals one, the driving force for crystallization is given by

$$\frac{\Delta\mu}{kT} = \ln \frac{a_i}{a_{i,eq}} = \ln \frac{\gamma_i m_i}{\gamma_{i,eq} m_{i,eq}} \approx \ln \frac{\gamma_i c_i}{\gamma_{i,eq} c_{i,eq}} \quad (4)$$

since for the molality m the concentration can be used for not too high concentrations. However, if crystallization involves a chemical reaction:



with A_i the starting components, B_j the reaction prod-

ucts, and S_{cr} the crystalline phase, then

$$\frac{\Delta\mu}{kT} = \sum_{i=1}^n \ln \frac{a_{A_i}}{a_{A_i,eq}} - \sum_{j=1}^m \ln \frac{a_{B_j}}{a_{B_j,eq}} \quad (6)$$

Dissolution of gibbsite in caustic solutions leads to the formation of several ions and soluble complexes.^{14–16} Single aluminum complexes, like AlO_2^- and $AlO(OH)_2^-$, dialuminum complexes, like $Al_2O(OH)_6^{2-}$ or the double hydroxy complex $Al_2(OH)_8^{2-}$, but also even higher aluminum complexes, like $Al_6(OH)_{24}^{6-}$, are supposed to be formed in sodium aluminate solutions. The driving force for gibbsite crystallization is determined by the activity of all these possible species related to the crystallization process. Recent studies showed that most of the dissolved aluminum is present as the aluminate ion, $Al(OH)_4^-$.¹⁷ Depending on the caustic concentration, this ion is hydrated at low caustic concentration or forms an ion pair with sodium at high caustic concentration.^{17,18} Significant concentrations of other single aluminium complexes, like AlO_2^- , were found to be negligible, although $Al_2O(OH)_6^{2-}$ dimers might be present in the solution.¹⁷ Here, it is assumed that besides $Al(OH)_4^-$, the concentration of all these species is negligible, so that the overall crystallization process corresponds to the reaction:



Using eq 6, it follows that the driving force for gibbsite crystallization equals:

$$\begin{aligned} \frac{\Delta\mu}{kT} &= \ln \frac{a_{Al(OH)_4^-}}{a_{Al(OH)_4^-,eq}} - \ln \frac{a_{OH^-}}{a_{OH^-,eq}} \\ &= \ln \frac{a_{Al(OH)_4^-}}{a_{Al(OH)_4^-,eq}} \frac{a_{OH^-,eq}}{a_{OH^-}} \approx \ln \frac{\gamma_{Al(OH)_4^-} [Al(OH)_4^-]}{\gamma_{OH^-} [OH^-]} \frac{\gamma_{OH^-} [OH^-]_{eq}}{\gamma_{Al(OH)_4^-,eq} [Al(OH)_4^-]_{eq}} \end{aligned} \quad (8)$$

Note that for the molality the concentration is used. Since the activity coefficients of the different ions in the Bayer liquor are not measured and the Debye–Hückel expression is not applicable for these concentrated ionic Bayer liquors, it is assumed that in the region of interest the ratio of the activity coefficients does not change with concentration, i.e., $\gamma_{Al(OH)_4^-}/\gamma_{OH^-} \approx \gamma_{Al(OH)_4^-,eq}/\gamma_{OH^-,eq}$. Then, the driving force is given by

$$\frac{\Delta\mu}{kT} = \ln \frac{c}{c_{eq}} \frac{[OH^-]}{[OH^-]_{eq}} \quad (9)$$

where c and c_{eq} are the actual and the equilibrium $Al(OH)_4^-$ concentration of the solution at the crystallization temperature T , respectively.

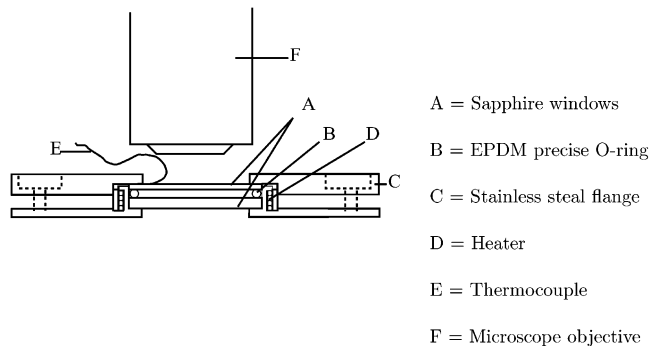


Figure 2. Experimental setup of the in situ cell.

Only if $(c/[OH^-])/(c_{eq}/[OH^-]_{eq})$ is close to unity, the driving force can be approximated by

$$\frac{\Delta\mu}{kT} \approx \sigma = \frac{\frac{c}{[OH^-]} - \frac{c_{eq}}{[OH^-]_{eq}}}{\frac{c_{eq}}{[OH^-]_{eq}}} \quad (10)$$

which is the relative supersaturation. In this relation, the assumption is made that $\ln(1 + \sigma) \approx \sigma$, which actually is only valid if σ does not exceed 10%. However, in case of gibbsite crystallization the supersaturation can exceed 100%.

Since no better information is available on the activities and the relevance of all minor species present in the solution participating in gibbsite crystal growth, the driving force defined by eq 9 is suggested to be the best possible definition of the gibbsite crystallization driving force, despite the fact that some assumptions have been made.

Experimental Section

In Situ Cell. To develop a suitable cell for in situ optical microscopy of gibbsite crystallization from the highly aggressive Bayer liquors at elevated temperatures, major problems have to be overcome. First, the cell may not contain metal or glass parts in contact with the liquid, as this leads to corrosion and contamination. Second, the temperature should be controlled within ± 2 °C. In addition, transmission optical microscopy has to be used to obtain clear in situ images. This requires two opposite optical windows. Attempts using cells made of resistant materials, like Teflon, failed because of leakage as a result of deformation at elevated temperatures and creeping of the liquid. Therefore, we were not able to construct a large volume cell or a flow system that should give control of the supersaturation during a complete growth run. As a consequence we had to resort to the cell described below. Although it fulfills all requirements, its volume is limited. This implies that supersaturation is only well defined at the beginning of each growth run, and a complete in situ run has to be carried out for each point of the growth rate versus supersaturation curve. This makes the experiments time consuming. The in situ growth experiments were done in a growth cell as is represented in Figure 2. To avoid corrosion by the caustic solution, the cell consists of two parallel, optically flat, sapphire windows separated by 1.5 mm by a precise, chemically resistant EPDM O-ring. The windows are clamped by stainless steel flanges, leaving an aperture of 2 cm. The volume of the cell is about 0.5 mL. The cell is heated from its outer wall, in which a coaxial resistance wire, connected to a power supply, is mounted.

The temperature for all experiments was 80 °C. The temperature of the cell was controlled by a thermocouple

Table 2. Liquor Specifications for the In Situ Experiments^a

C_i g/L Na_2CO_3	$(A/C)_i$	C_{eq} g/L Na_2CO_3	$(A/C)_{\text{eq}}$	$\Delta\mu/kT = \ln(c/[\text{OH}^-]) / (c_{\text{eq}}/[\text{OH}^-]_{\text{eq}})$ (eq 9)	$\sigma = (c/[\text{OH}^-] - c_{\text{eq}}/[\text{OH}^-]_{\text{eq}}) / (c_{\text{eq}}/[\text{OH}^-]_{\text{eq}})$ (eq 10)
100.13	0.500	101.57	0.311	0.82	1.27
103.31	0.597	105.64	0.313	1.22	2.40
100.22	0.599	102.45	0.311	1.24	2.45
100.99	0.679	103.91	0.312	1.61	3.99
101.06	0.683	104.01	0.312	1.63	4.09
104.44	0.694	107.67	0.314	1.68	4.35
100.01	0.698	103.03	0.312	1.71	4.52
100.00	0.700	103.04	0.312	1.72	4.58
96.03	0.714	98.96	0.309	1.80	5.06
197.32	0.479	200.29	0.368	0.47	0.60
197.35	0.515	201.32	0.369	0.62	0.85
198.81	0.529	203.21	0.370	0.67	0.96
201.99	0.592	208.38	0.374	0.93	1.52
200.29	0.599	206.83	0.373	0.96	1.61
205.96	0.628	213.67	0.377	1.07	1.91
205.96	0.628	213.67	0.377	1.07	1.91
198.01	0.692	207.51	0.373	1.40	3.05
198.54	0.697	208.07	0.373	1.42	3.15
199.91	0.699	209.61	0.374	1.43	3.18
200.37	0.699	210.11	0.375	1.43	3.18
200.13	0.701	209.91	0.375	1.44	3.22
207.28	0.738	218.91	0.380	1.62	4.04
200.44	0.796	213.49	0.377	2.01	6.47
200.00	0.800	213.12	0.377	2.04	6.68
200.00	0.801	213.16	0.377	2.05	6.74
298.87	0.487	301.69	0.438	0.21	0.23
300.24	0.598	309.81	0.444	0.65	0.92
299.34	0.697	315.65	0.448	1.11	2.02
298.41	0.697	314.69	0.447	1.11	2.03
303.97	0.701	320.8	0.452	1.11	2.03
300.00	0.700	316.56	0.449	1.12	2.06
302.52	0.783	325.56	0.455	1.58	3.87
300.88	0.799	325.03	0.455	1.70	4.47
300.09	0.800	324.21	0.454	1.71	4.52
300.00	0.800	324.13	0.454	1.71	4.52
298.41	0.806	322.85	0.453	1.76	4.80

^a C is the caustic concentration expressed in g/L Na_2CO_3 , and A is the aluminum hydroxide concentration expressed in g/L Al_2O_3 . C and c_{eq} are the actual aluminum hydroxide concentration and the equilibrium value, respectively. The temperature for all experiments is 80 °C.

mounted on the upper window just below the stainless steel flange, combined with a temperature controller with a stability of ± 0.1 °C. Unfortunately, it was not possible to measure the temperature inside the cell during the experiments, since the high caustic concentration of the Bayer liquors would destroy the thermocouple. Using the same setup filled with water, the temperature in the cell was determined to be almost similar to the temperature measured by the thermocouple. A small difference of less than one degree was present. It is supposed that there is also a temperature difference between the periphery and the center of the cell. Measurements outside the cell between these two points revealed a difference of less than two degrees, which is explained by the relatively high thermal conductivity of the sapphire windows. This radial temperature gradient is expected to be lower inside the cell, because the thermal resistance of the windows causes less heat to dissipate and thus stabilises the temperature. As a result of this small temperature difference, some convection is expected to occur in the cell.

At the beginning of each experiment, 0.4 mL of Bayer liquor at a temperature of about 60 °C was put on the lower sapphire window, which was preheated. Here, care was taken that the solution did not contact the O-ring, enabled by the high surface tension of the liquid. After this, the upper window was placed on top. The amount of liquor was chosen such that after closing the cell the liquor contacted both sapphire windows, allowing for a small air bubble to be present. In this way, light scattering from a liquid–air boundary otherwise present was prevented and, in addition, pressure changes, due to the volume changes as a result of the crystallization process and due to the heating of the liquor, were suppressed by the air bubble. After closing the cell, it took only a few minutes to reach the desired temperature. It is estimated that a temperature difference of $\pm 2^\circ$ introduces an error in the driving force calculation of ± 0.06 .

Bayer Liquors. Pure Bayer liquors were prepared by dissolving aluminum (purity 99.999%) in about 50 mL of concentrated sodium hydroxide (p.a.) solutions at 90–100 °C in a Teflon vessel. In doing this, safety precautions had to be taken in view of the high caustic concentration of the solution, the increase of the temperature due to the exothermic reaction, and the generation of H_2 gas. After complete dissolution of the aluminum, the solutions were filtered through a Millipore HVLP 0.45 μm filter and diluted with deionized water to obtain the desired caustic and aluminate concentration.

Different conditions for gibbsite nucleation and growth were obtained by varying the caustic concentration and the sodium aluminate concentration. Three different caustic concentrations were used, namely, $C = 100, 200,$ and 300 g/L Na_2CO_3 in terms of the alumina refinery notation (one mole of Na_2CO_3 corresponds with two moles of NaOH). These values correspond to a NaOH molarity of 1.89, 3.77, and 5.66 mol/L, respectively. The aluminate-to-caustic ratio A/C varied from 0.5 to 0.8, where A represents the aluminate concentration expressed in grams per liter Al_2O_3 . The liquor specifications of all experiments are given in Table 2.

For a conversion between the conventional and alumina refinery notation see, e.g., ref 19.

The equilibrium caustic and alumina concentrations were determined using a computer algorithm, which is based on an equation derived by McCoy et al.,²⁰ relating the equilibrium solubility of gibbsite to the temperature, caustic concentration and impurity concentrations of sodium aluminate liquors. The error in the driving force, due to errors in weighing the NaOH and Al pellets, is ± 0.01 . This is far less than the ± 0.06 error introduced by an error in temperature in the in situ cell due to a possible temperature gradient between the periphery and the center of the cell. The series of experiments are referred to their C and A/C values.

Seeds. Both seeded and unseeded growth experiments were done. Seed material was prepared in the *in situ* cell under similar conditions as the experiments. Crystallites nucleated on the sapphire windows and remained stuck to the window after opening the cell. These crystals were immediately used as seeds in a fresh solution, without washing and drying of the adhering solution and therefore not coming into contact with air. In this way, possible effects of surface restructuring (measurable as an induction period prior to nucleation and growth) were reduced to a minimum. As a result of this preparation method, a thin liquid layer remained on the sapphire window and seeds, which could have slightly affected the actual aluminate supersaturation. However, the amount of this liquid was so small that its influence is negligible. The above procedure was carried out as quickly as possible, thereby minimizing the reaction with atmospheric CO_2 producing Na_2CO_3 in the liquor. In this way, traces of Na_2CO_3 in the Bayer liquor, which might affect the growth kinetics, were kept as small as possible.

Observations and Measurements. The growth of the crystals was followed in time using a transmission optical microscope (Olympus Vanox), fitted with a long working distance ($20\times$, $NA = 0.40$) objective corrected for observation through the window and liquid. Crystal growth rates were determined by capturing images at selected time intervals (typically, 10–30 min, depending on the growth rate) using a digital video camera connected to a computer. The linear growth rate of the crystal faces was calculated from the increase in crystal size after each time interval, which was measured by determining the distance between two opposite faces of the same type.

For all experiments given in Table 2, the growth rates of seeds and spontaneously formed nuclei were measured, distinguishing the individual crystal faces. For the single crystalline lozenges, it was shown that the $\{110\}$ faces dominate the growth morphology, while for the 6-fold twinned hexagons, the $\{100\}$ faces are the most prominent side faces.¹⁰ Therefore, the $\{100\}$ and basal $\{001\}$ faces of 6-fold twinned hexagons, the $\{110\}$ and some $\{100\}$ faces of lozenges and the $\{001\}$ and side faces of prismatic crystals were examined. For the prisms, it was not clear whether the $\{100\}$ or $\{110\}$ faces were the side faces. After completing the growth experiments, the crystals were separated from the solution, and the occurrence of twinning was verified with polarization microscopy. This was not possible during the experiments, because the use of single crystalline, birefringent sapphire windows prevented observation of twinning with polarization microscopy. As expected, this revealed that the larger hexagons were twinned 6-fold along the $\{110\}$ faces. For the prisms, 6-fold twinning parallel to the c -axis could not be detected, because viewing the prisms perpendicular to c the separate crystal domains have the same extinction direction. Single twinning parallel to $\{100\}$ and twinning perpendicular to the c -axis were not observed for prisms in the *in situ* cell.

In each experiment, usually 3–10 crystals of one kind (twinned hexagons, single crystalline lozenges, or prisms) were measured in all possible crystallographic directions. It was found that the growth rates of crystal faces were more or less identical for the symmetry equivalent crystal faces of one crystal, but varied a lot between different crystals. The growth rate of each single crystal was, therefore, determined by averaging the growth rates in these equivalent directions. In this way, the error in growth rate for each experiment was estimated from the errors in growth rates of each individual crystal. The error in measuring the increase in size of each crystal was $\pm 0.35 \mu\text{m}$. Depending on the time between each measurement of the crystal sizes, this leads to an error in growth rate of 0.4–2.0 $\mu\text{m}/\text{h}$. The measurements perpendicular to the c -axis of crystals oriented with the $\{001\}$ axis perpendicular to the optical axis of the microscope were somewhat less precise since the crystal boundaries were slightly out of focus. It was found that the dispersion in growth rate of the individual crystals gives rise to fluctuations in growth rate larger than the experimental error. The final growth rates of each type of face were, nevertheless, obtained by averaging

over all crystals growing in the same experiment, thus, averaging the effect of growth rate dispersion.

Since the cell consisted of a closed compartment, the overall supersaturation of the solution decreased as nucleation and crystal growth proceeded. As a consequence, the crystal growth rate decreased in time. Because of the small volume of the *in situ* cell, it was not possible to carry out liquor analysis during and after the experiment. Therefore, only the initial liquor specification was known. The average maximal growth rate at the beginning of each experiment, that is, after a short induction period, is used as the actual growth rate corresponding to the growth conditions chosen. As a result of an increase in growth rate after this induction period, which will be described in a subsequent section, this value will be slightly too low. It is, however, expected that this deviation is only small and that its effect on the growth rate is less than the other errors of the experiments. The growth rates measured as a function of the driving force are fitted to various growth rate equations using a least-squares fit method.

Results

Growth Velocity Measurements. A typical seeded growth sequence, imaged by *in situ* optical microscopy, is shown in Figure 3. The conditions were $C = 200 \text{ g/L Na}_2\text{CO}_3$, $A/C = 0.8$, and $T = 80^\circ\text{C}$. The sequence clearly shows the increase in size of the seed crystals in time and simultaneously the formation and growth of new nuclei. The seeds as well as the nuclei formed have either a hexagonal or a lozenge-shaped morphology. Depending on their orientation on the sapphire window the crystals are viewed parallel or perpendicular to the c -axis.

Following these crystals in time and measuring the linear growth rates resulted in typical growth curves as shown in Figure 4. The error bar is estimated to be about 2 $\mu\text{m}/\text{h}$ for each measurement. This diagram represents the growth rates of the $\{100\}$ faces of two hexagons measured in time in three equivalent $\langle 100 \rangle$ directions. From these curves, it is clear that the three different $\langle 100 \rangle$ directions of each hexagon have more or less identical growth rates, although they fluctuate in time. Different crystals in the same run mutually vary a lot in growth rate. The thicker curve represents the mean value of measurements of six hexagons of the same experiment, either seeded or freshly nucleated. It should be noted that on the average the growth rates of the seeds and freshly nucleated crystals did not differ. In general, the growth rate decreased in time, which is expected since the supersaturation decreased in the closed cell system.

The development of fresh nuclei does not affect the supersaturation at the moment of maximal growth rate for $C = 100$ and $C = 200 \text{ g/L Na}_2\text{CO}_3$. At this early stage of each experiment, the 3D nuclei are very small and therefore only consume a negligible amount of solute. For instance, in Figure 3b,c, which was recorded at the moment of maximal growth, the total surface area of the fresh nuclei is less than 3% of the total surface area of the seed crystals. For $C = 300 \text{ g/L Na}_2\text{CO}_3$; however, in some cases massive nucleation occurred at an early stage of growth. This affects supersaturation and may explain the large scatter in growth rate values for this caustic concentration.

During most experiments, after an initial increase the growth rate became maximal and then decreased slowly. This initial increase was observed for seeds as well as

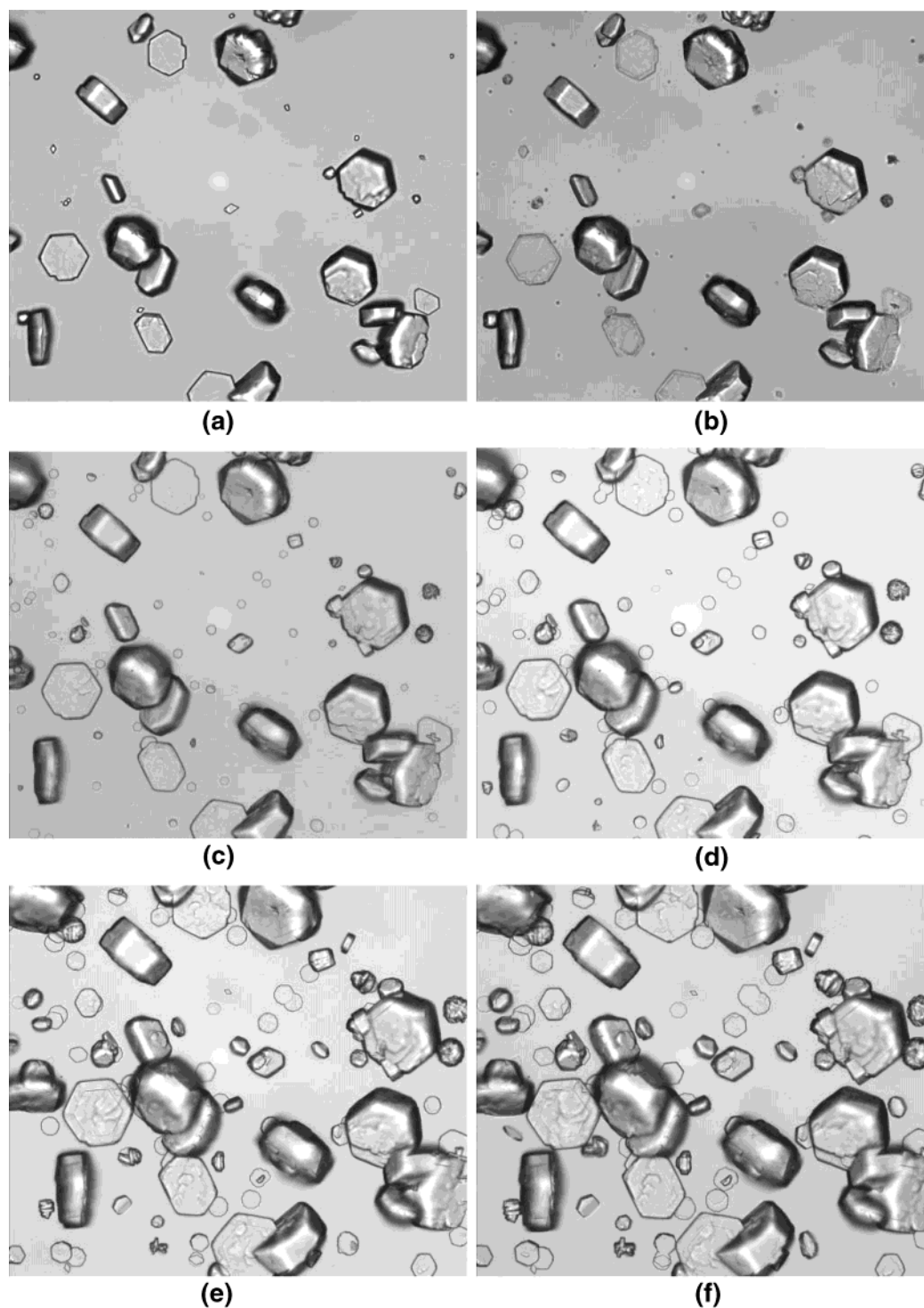


Figure 3. (a–f) Growth sequence of gibbsite crystals for conditions $C = 200$ g/L Na_2CO_3 and $A/C = 0.8$. The linear size of the images is $400 \mu\text{m}$ and $\Delta t = 10, 20, 35, 55, 95,$ and 135 min, relative to the starting time t_0 . In this sequence, seed crystals grow to larger crystals. The seeds are mainly hexagonally shaped, but also lozenges are observed. In addition, the formation of new nuclei can be seen.

for the nuclei formed immediately at the beginning of an experiment. The time of increase depends on the driving force: the higher the driving force the shorter its length. It was independent of the warming-up time of the in situ cell, which took maximally 2 min. However, also for this dependency a large dispersion was found. The occurrence of an induction period prior to growth is sometimes explained by surface restructuring of the seed crystals.²¹ In that case, however, nuclei freshly formed should not show this effect. One may

speculate, therefore, that the induction period corresponds with the time of solution restructuring, necessary for growth, which still takes place after raising the temperature of the cell to the experimental value. The induction period may also be introduced by very low concentrations of Ca^{2+} in the liquor, as was reported in the literature.²² These traces of Ca^{2+} can lead to some of the observed growth rate dispersion, as well.

Figure 5 shows the average linear growth rates of individual faces of the gibbsite single-crystal faces as a

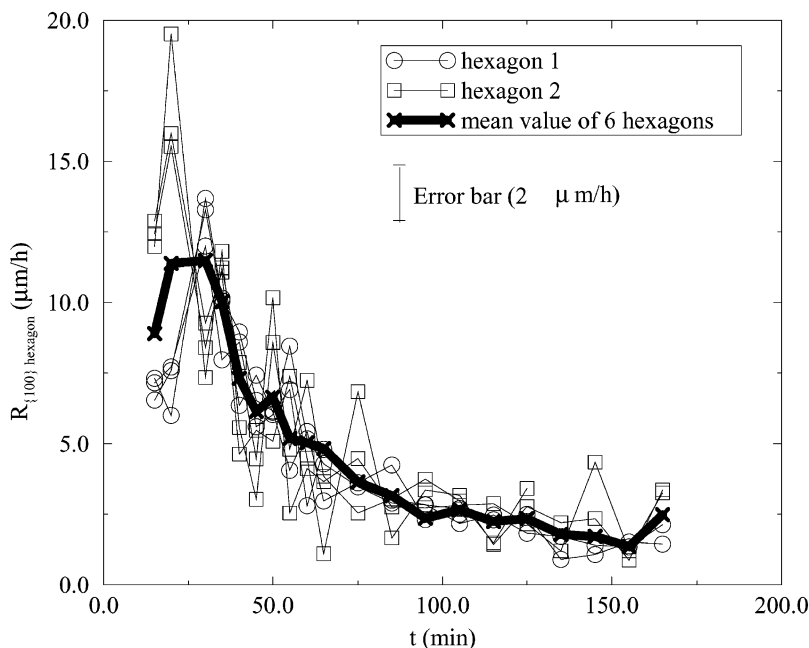


Figure 4. Typical growth rates of $\{100\}$ side faces of hexagons in one experiment versus time for $C = 200$ g/L Na_2CO_3 and $A/C = 0.8$. The numbers 1 and 2 refer to the growth rates of two hexagons each measured along the three equivalent $\langle 100 \rangle$ directions. The thick line refers to the mean value of six hexagons, either seeded or freshly nucleated. The growth rate decreases in time, although at the beginning of the experiment an increase can be seen. Another characteristic is that the three faces of each hexagon show similar fluctuations of the growth rate in time.

function of the driving force, expressed as $\Delta\mu/kT = \ln(c/[\text{OH}^-])/(c_{\text{eq}}/[\text{OH}^-]_{\text{eq}})$ (eq 9). Each point corresponds with an individual in situ run. As was explained in Experimental Section, the maximum value of the average growth rate curve of each run was chosen as the actual growth rate belonging to the growth conditions concerned. In Figure 5d,e, the growth rate data of King for which C varied from 120 to 220 g/L Na_2CO_3 are also presented.⁴

Some general trends can be recognized. The figure indicates that higher growth rates are obtained at higher supersaturation. Further examination of the growth rates shows that large variations in average crystal growth rates are obtained for different gibbsite crystals under identical conditions, but in different experiments. In general, the growth rate for the different faces follows the sequence: $R_{\{100\},\text{hexagon}} > R_{\{110\},\text{lozenge}} > R_{\{001\},\text{hexagon}}$. This behavior in growth rate of faces corresponds to the results of a previous paper, in which the morphological importance of the faces was found to follow $MI_{\{001\}} > MI_{\{110\}} > MI_{\{100\}} > MI_{\{112\}} \approx MI_{\{101\}}$.¹⁰ The growth rates of the $\{100\}$ and side faces of prismatic crystals measured by King are similar to our growth rates measured for the $\{100\}$ faces of the hexagons. However, the growth rates obtained for prismatic crystals in the $\langle 001 \rangle$ and lateral directions were smaller in our case. The results obtained by Lee et al.⁹ differ from our results, which is possibly because they measured relative growth rates.

Characteristic Features. Observations reveal that at low driving force lozenge-shaped crystals became truncated by the appearance of small $\{100\}$ faces. At high driving force, these faces grew relatively faster and lozenges were formed again. This implies that at low driving force the linear growth rate of the $\{100\}$ faces

is slightly less than $\sqrt{3}$ times the linear growth rate of the $\{110\}$ faces, while at higher driving force the linear growth rate of $\{100\}$ becomes dominant. The formation of nontwinned hexagonal crystals is the result of equal growth rates in the $\langle 110 \rangle$ and $\langle 100 \rangle$ directions. Such crystals have been observed, but were rare. A crossover point at low driving force for the growth rates of $\{100\}$ and $\{110\}$ faces is theoretically possible, resulting in hexagons elongated along b .

Another interesting growth phenomenon is shown in Figure 6. It shows a 6-fold twinned hexagonal seed with reentrant corners. The growth mechanism of such twinned hexagons is the combination of fast growing $\{100\}$ faces and a twin plane reentrant corner induced 2D nucleation growth of the adjacent $\{110\}$ faces.¹⁰ In this sequence, it is shown that the reentrant corners become smaller in time. Hence, at the beginning, when the supersaturation is higher, the growth rate of the $\{100\}$ faces is faster than the growth rate of the $\{110\}$ faces induced by 2D nucleation growth at the reentrant corners. Later in the experiment, when the supersaturation is decreased, the growth rate of the $\{100\}$ side faces becomes comparable to that of the adjacent $\{110\}$ faces. When the reentrant corner is almost vanished, the growth rate ratio of the $\{100\}$ side faces and the advancement rate of the reentrant corner is exactly 2: $\sqrt{3}$, as concluded from geometrical considerations. In other words, the growth rate of the associated $\{110\}$ faces is identical to that of the $\{100\}$ faces. Note that the $\{110\}$ side faces of the adjacent lozenge grow at a much reduced rate. This can be explained by the absence of reentrant corners as step sources. However, such a very large difference in growth rate between the $\{100\}$ and $\{110\}$, i.e., 1.0 versus 0.1 $\mu\text{m/h}$, respectively, was not observed in other experiments.

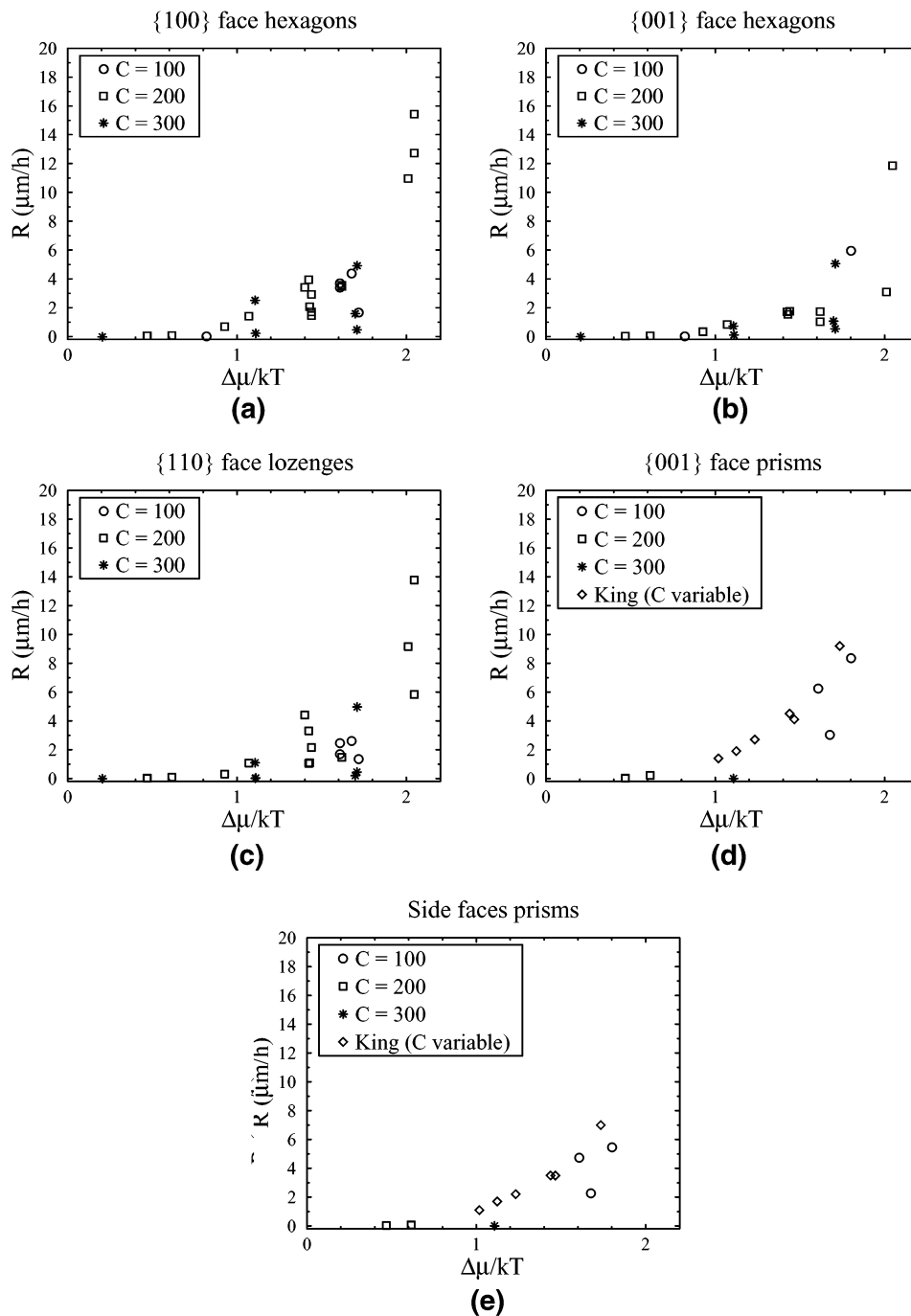


Figure 5. The linear growth rates of gibbsite crystal faces versus $\Delta\mu/kT$ as defined in eq 9, for (a) the {100} and (b) the {001} faces of hexagons, (c) the {110} faces of lozenges, and (d) the {001} and (e) the side faces of prisms. It is not clear whether the side faces of the prisms were {110} or {100} faces. It should be noted that each point in the graphs does not correspond with the growth rate of a particular crystal, but is the growth rate of the face in a given crystallographic direction averaged over several crystals in one experiment. In graphs (d) and (e), the data of King⁴ are also represented.

Discussion

Crystal Growth Rate Dispersion. The aim of this study is to find the relation between the growth rate of a gibbsite crystal face and the driving force. In general, it is assumed that the crystal growth rate is only determined by the driving force, and that there is an unambiguous relationship between crystal growth rates and the driving force for each face $\{hkl\}$. However, in case of the crystallization of gibbsite it is observed that the crystal growth rates can differ as much as 100% for

crystals in the same experiment and that these fluctuate fairly in time, despite the fact that the temperature of the cell is constant. This can also not be explained by a local fluctuation in driving force due to heat or mass transport, since it is supposed that gibbsite crystal growth is surface reaction controlled^{3,23} and the overall driving force is supposed to be constant everywhere in the cell, only decreasing in time. Furthermore, the average crystal growth rates differ a lot under apparently identical crystallization conditions. A small part of the variation in growth rate can be explained by

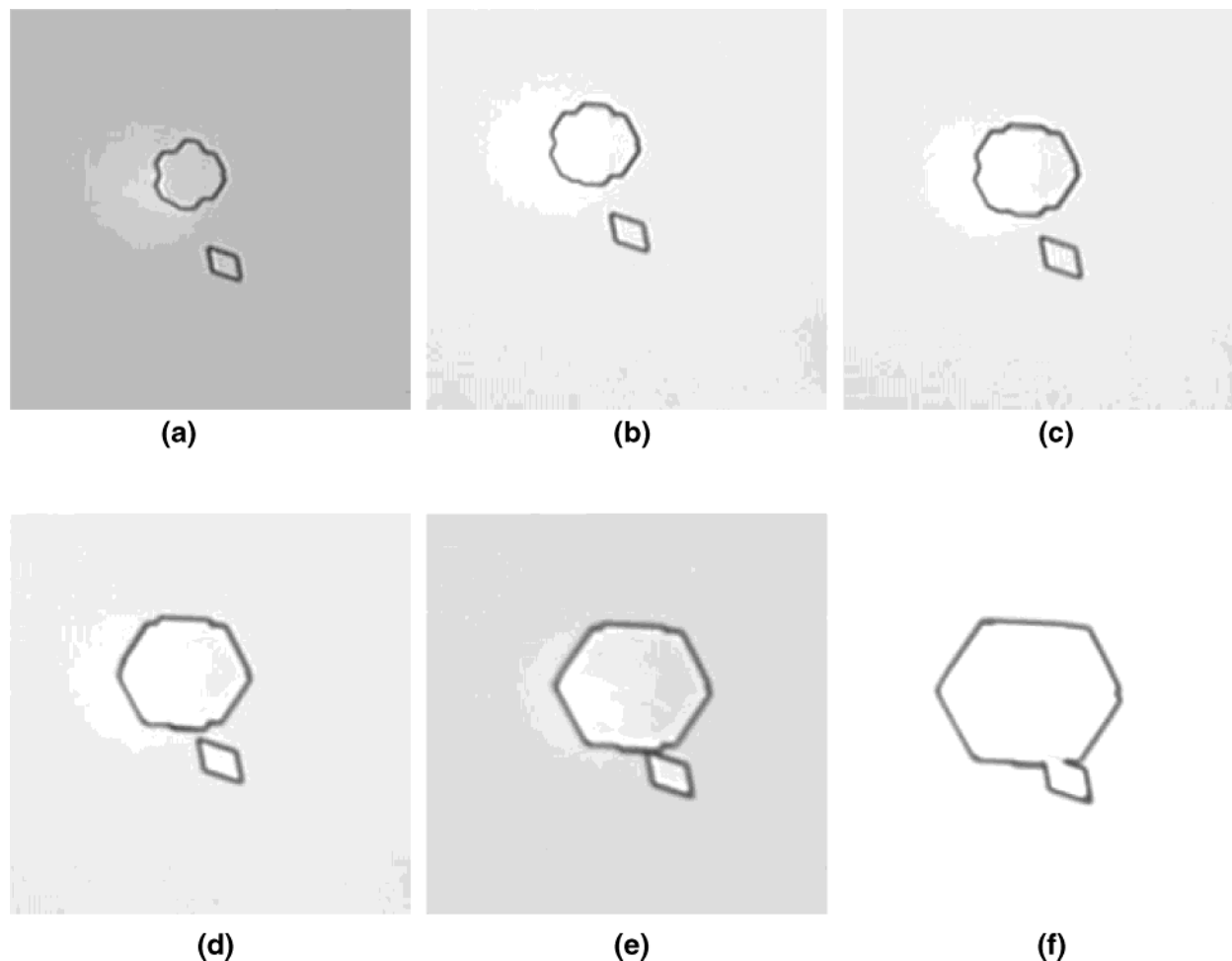


Figure 6. Growth sequence of a 6-fold twinned hexagon with reentrant corners at $C = 200$ g/L Na_2CO_3 and $A/C = 0.8$. The time sequence is (a) 0 h, (b) 1 h, (c) 2 h, (d) 4 h, (e) 6 h, and (f) 9 h. The width of the reentrant corner decreases in time. This suggests that at lower supersaturation, i.e., after longer time, the crystal growth mechanism induced by the reentrant corner becomes more important relative to the growth at the $\{100\}$ side faces. The size of the pictures is $80 \times 80 \mu\text{m}$.

errors in determining $\Delta\mu/kT$ and in measuring the crystal sizes; the remaining part must be real variations in growth rates of crystals. It is estimated that the error in determining the driving force is ± 0.06 , which is mainly caused by a temperature gradient in the cell. The error in crystal growth rate measurements is $0.4\text{--}2 \mu\text{m/h}$. The variation in growth rate of different crystals and in time within one and different experiment(s) is clearly larger than $2 \mu\text{m/h}$, indicating that the dispersion of crystal growth is not induced by the inaccuracy of the measurements, but indeed is related to physical properties of the crystals or the solution. The observation of crystal growth dispersion as an intrinsic characteristic of the material is supported by other studies of crystallizing compounds including gibbsite.^{7,9} These variations seem to increase at higher temperature and higher driving force,⁷ which is also the case in our experiments.

According to classical theories,⁷ crystal growth rate dispersion can be explained by (1) size-dependent growth related to a Gibbs–Thomson effect, (2) the variation in number and activity of dislocation and other step sources at the crystal surface, (3) the overall lattice strain of crystals, or (4) impurity effects.

The Gibbs–Thomson effect suggests that if growth is controlled by a surface integration mechanism, small

crystals grow more slowly than larger crystals. This effect is explained by a difference in solubility as a function of crystal size.⁷ According to this model, the size dependent growth is only relevant for crystals with sizes close to the size of a critical nucleus, because the effective driving force experienced by the crystals is given by

$$\Delta\mu_{\text{eff}} = \Delta\mu_{\text{app}} \left(1 - \frac{r_c}{r} \right) \quad (11)$$

In this equation, $\Delta\mu_{\text{app}}$ is the applied driving force, r is the size of a crystal and r_c is the size of a 3D critical nucleus. If the size of a critical nucleus is about 1.2 nm, as suggested by Rossiter et al.,²⁴ the observed crystals larger than $1 \mu\text{m}$ lead to a $\Delta\mu_{\text{eff}}$ that approximates $\Delta\mu_{\text{app}}$ and, thus, this size effect is negligible for gibbsite crystal growth. Some authors proposed a size-dependent growth mechanism for gibbsite crystallization,⁹ whereas others did not observe any size-dependent growth.³ The latter corresponds with our observations, where also crystals of the same size have different growth rates, which, in addition, fluctuate in time.

The cause of growth rate dispersion for gibbsite possibly lies in the changing activity of dislocations or of a group of dislocations emerging at the surface during

crystal growth. An alternative may be the deposition of microcrystallites on the crystal surface leading to varying rates of step generation by contact nucleation. On the other hand, it is observed that the faces of one crystal have the same fluctuation behavior, which would suggest that the growth rate dispersion is more related to local solution specifications. One may speculate that solvent restructuring as part of the growth mechanism leads to dispersions in growth rates.^{16,21} Another factor influencing crystal growth is the presence of small amounts of impurities at the growing interface. These particles can adsorb on the surface and influence the step flow on crystal surfaces. This can finally lead to discontinuous growth, even followed by periods of stagnation. In addition, point defects may result in microscopic lattice stress centers which may cause disorder (mosaicity) of crystals and retardation or cessation of growth. A surface topographic study of gibbsite crystals published elsewhere¹¹ shows that in gibbsite crystals many defects are present, which also result in different step sources on crystal surfaces, stress, and even mosaicity. It was also proposed that impurities have a large influence on the gibbsite growth mechanism. However, the results of the present study cannot lead to a decisive conclusion concerning the cause of the growth rate dispersion.¹⁰

Relevant Growth Rate Equations. (i) Influence of Caustic Concentration on Growth Rate. In Figure 5, the results of the average growth rates are plotted versus the applied driving force defined by $\Delta\mu/kT = \ln(c[\text{OH}^-]/(c_{\text{eq}}/[\text{OH}^-]_{\text{eq}}))$. Using this definition, the data suggest that the caustic concentration is no longer involved. However, it should be realized that for $C = 300$ g/L Na_2CO_3 the number of data points is limited and the scatter is high. If the driving force would be expressed as $\Delta\mu/kT = \ln c/c_{\text{eq}}$, the difference in the experimental data points for different caustic concentrations was clearly visible. The scatter at $C = 300$ g/L Na_2CO_3 largely results from the massive nucleation that took place in a number of cases, making it difficult to determine the growth rates of the individual crystals properly (see Figure 7).

Compared to the very high caustic concentrations, the data points for the lower C (100 and 200 g/L Na_2CO_3) are better. The most reliable growth rates measured in this study are for the $\{100\}$ faces of the hexagons and the $\{110\}$ faces of the lozenges at $C = 200$ g/L Na_2CO_3 . Therefore, these data are used to determine the crystal growth mechanism in the next section. The data points measured for the prisms are not used, because of their limited number. Instead, the data points of King⁴ are used to analyze the growth mechanism for prisms.

(ii) Relevant Growth Mechanisms. It is well-known that the growth rate of crystals can be controlled by transport processes, i.e., mass transport of growth units from the solution toward the crystal surface. In the case of gibbsite growth, this is not the rate-limiting crystallization step because of the slow growth rates of gibbsite even if the solution is agitated well. In addition, diffusion controlled growth is proportional to the difference between the actual and equilibrium solute concentration, $c - c_{\text{eq}}$, which is certainly not the case regarding the curves in Figure 5. Therefore, surface integration rather than mass transport is expected to

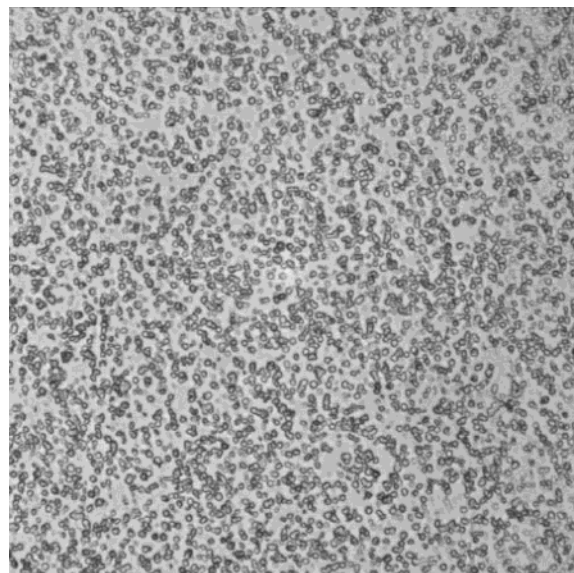


Figure 7. In situ image showing massive nucleation of crystals at $C = 300$ g/L Na_2CO_3 , at the moment of maximal growth rate. The magnification is the same as in Figure 3.

control gibbsite crystal growth. This agrees with the conclusions as reported in the literature, which were deduced from the very low growth rate (a few $\mu\text{m/h}$), the square law relationship between the growth rate and supersaturation (i.e., if $S = \sigma$), the high activation energy for growth, and the negligible effect of agitation on the growth rate.^{3,23} If transport is not relevant, mononuclear and polynuclear two-dimensional (2D) nucleation can dominate gibbsite growth, but also a dislocation mechanism is possible. Examination of the surfaces of gibbsite crystals by optical and atomic force microscopy reported earlier demonstrated that the $\{001\}$ faces of 6-fold twinned hexagons grow by a dislocation and a contact nucleation mechanism as do the $\{001\}$ faces of prisms.¹¹ In that study, two kinds of lozenges have been distinguished: *ultrathin* lozenges and *thicker* lozenges of which the $\{001\}$ basal faces grow by a 2D nucleation and a dislocation mechanism, respectively. The $\{110\}$ side faces of both types of lozenges turned out to grow by a polynuclear birth and spread mechanism. The $\{100\}$ side faces of the hexagons and prisms grow by a polynuclear birth and spread mechanism, in which the growth of the side faces of prisms was suggested to be affected by impurities or stress due to mosaicity formation. A mononuclear birth and spread mechanism is very unlikely in the above cases, because the surfaces are relatively large and the AFM topographic studies indicated polynuclear birth and spread.

(iii) Growth Rate Equations. In the field of industrial crystallization, the $R(\Delta\mu/kT)$ dependence is usually approximated by the power law form:

$$R = k_0 S^p \quad (12)$$

where p is the kinetic order, and k_0 is the kinetic coefficient. If the results presented in Figure 5 are fitted to this equation using $S = \Delta\mu/kT = \ln((c[\text{OH}^-])/(c_{\text{eq}}/[\text{OH}^-]_{\text{eq}}))$, then the kinetic order p varies from 4.5 to 6.7. If for $S \sigma = (c[\text{OH}^-] - c_{\text{eq}}/[\text{OH}^-]_{\text{eq}})/(c_{\text{eq}}/[\text{OH}^-]_{\text{eq}})$ is used, for the $\{100\}$ faces of the hexagons, the $\{110\}$ faces of the lozenges and the $\{001\}$ and $\{\text{side}\}$ faces of Kings

crystals, p is about 2. This would suggest that spiral growth is the plausible mechanism for gibbsite crystallization. However, the equation $R = k_0 S^2$ for spiral growth is only valid at low supersaturation, which is usually not applied in gibbsite crystallization. Furthermore, the growth mechanism cannot be described by the above quadratic equation, since the definition of the driving force $\sigma = (c/[\text{OH}^-] - c_{\text{eq}}/[\text{OH}^-]_{\text{eq}})/(c_{\text{eq}}/[\text{OH}^-]_{\text{eq}})$ is not the correct one, as is concluded in the previous section.

If growth is controlled by a polynuclear birth and spread mechanism, according to Nielsen,¹ the growth rate equation at higher driving force $\Delta\mu$ is given by:^{7,8}

$$R_p = A_1 \left(\exp\left(\frac{\Delta\mu}{kT}\right) \right)^{7/6} \left(\exp\left(\frac{\Delta\mu}{kT}\right) - 1 \right)^{2/3} \left(\frac{\Delta\mu}{kT} \right)^{1/6} \times \exp\left(\frac{-A_2}{\Delta\mu/kT}\right) \quad (13)$$

with A_1 and A_2 constants that are independent of the driving force. If the growth of a crystal face is associated with crystal dislocations, the rate of growth is expressed by²⁵

$$R_d = B_1 \left(\exp\left(\frac{\Delta\mu}{kT}\right) - 1 \right) \frac{\Delta\mu}{kT} \tanh\left(\frac{B_2}{\Delta\mu}\right) \quad (14)$$

with B_1 and B_2 independent of $\Delta\mu/kT$.

An AFM study¹¹ showed that an important step source for gibbsite crystallization is contact nucleation introduced by misoriented crystallites at the surface. To derive an expression for growth by contact nucleation, the theory for multiple birth and spread nucleation is applied to a linear edge, which presents the intersection line of the foreign crystallite and the growing crystal surface. The complete derivation is given in the appendix. The main result is the equation:

$$R_c = C_1 \left(\exp\left(\frac{\Delta\mu}{kT}\right) - 1 \right)^{1/2} \exp\left(\frac{\Delta\mu}{kT}\right) (\Delta\mu)^{-1/2} \exp\left(\frac{-C_2}{\Delta\mu}\right) \quad (15)$$

where C_1 is a constant and $C_2 = \gamma_s^2 \Omega^{2/3} / 2kT (\theta - 1/2 \sin(2\theta))$.

Fit Procedure and Discussion. The growth rate expressions for crystal growth determined by a birth and spread mechanism, dislocation growth, and contact nucleation, as given by the eqs 13–15, were used to find which growth mechanism is most plausible for the individual faces of gibbsite crystal growth.

In Figure 8 the curve fitting results for the three growth mechanism equations are presented for the {100} faces of hexagons, {110} faces of lozenges, and the {001} and side faces of King's prismatic crystals. The data fit to some extent to the spiral growth mechanism, but visual inspection of the graphs show a far better fit for the birth and spread mechanism and the equation for the contact nucleation growth mechanism. Recently, Farhadi and Babaheidary arrived at the same conclusion, i.e., a prevalency for 2D nucleation in growth, by analysis of gibbsite growth rate curves obtained from batch crystallization experiments.²⁶

For the faces of different crystal types, the curves have roughly the same pattern. Some data points

Table 3. Edge Free Energies [J/m²], Calculated from the Constants A_2 and C_2 , Obtained by Fitting the Measured Growth Rates

face { hkl }	γ_s, A_2	γ_s, C_2
hexagon {100}	0.081	0.102
hexagon {001}	0.125	0.130
lozenge {110}	0.058	0.090
{001} King [4]	0.031	0.073
side faces King [4]	0.059	0.079
{001} Lee [9]	0.050	0.057
side faces Lee [9]	0.079	0.079

deviate from the curve. Besides crystal growth rate dispersion, this can also be the result of the occurrence of a different growth mechanism for a few individual cases. The results are compatible with the surface topography data available for the different faces. The {001} faces of the 6-fold twinned hexagons and prisms were found to grow by a multiple dislocation and a contact nucleation mechanism. The curve fitting suggests that the latter controls the overall growth rate. As the fits suggests, the {110} side faces of the lozenges, the {100} side faces of the 6-fold twinned hexagons and the side faces of prisms are controlled by a polynuclear birth and spread or contact nucleation mechanism. This agrees with the conclusions from our previous AFM study.

Estimation of the Edge Free Energy, γ_s . Analyzing the dependence of the growth rates R of crystals as a function of the driving force $\Delta\mu/kT$ does not lead to a definite conclusion on the actual growth mechanism of gibbsite. The edge free energy estimated from the fits may reveal which of the two possible mechanisms, 2D birth and spread or 2D contact nucleation, is plausible. The edge free energy is related to the growth rate R_d and R_c through the constants A_2 and C_2 . The relationship between A_2 , C_2 , and γ_s is described by

$$A_2 = \frac{\beta \gamma_s^2 \Omega^{4/3}}{3(kT)^2} \quad (16)$$

and

$$C_2 = \frac{\gamma_s^2 \Omega^{4/3}}{2(kT)^2} \left(\theta - \frac{1}{2} \sin(2\theta) \right) \quad (17)$$

In both equations, γ_s is in [J/m²]. The values of A_2 and C_2 were obtained from the fit procedure. The volume of the growth unit, Ω , was calculated as one-eighth of the unit cell volume and the geometrical factor, β , is taken equal to one. Further, it is assumed that $(\theta - 1/2 \sin(2\theta)) \approx 1$, or $\theta \approx 73^\circ$, which is the contact angle of the hemispherical step patterns introduced by contact nucleation, as imaged with AFM.¹¹ The calculated edge free energies γ_s at 80 °C for various gibbsite faces are listed in Table 3. For all faces, the γ_s values are in the order of 0.03–0.1 J/m². The order is similar to that estimated by Lee et al.⁹ (6.0 ± 1.5 kJ/mol, which corresponds to 0.07 J/m²) as well as to the value $\gamma \Omega^{-2/3} = 0.05$ J/m² (for $\phi = 7.7 \times 10^{-21}$ J/molecule) as obtained by Farhadi and Babaheidary from fitting the polynucleation model at 80 °C.²⁶ Table 3 also shows that γ_s is higher for {001} than for {110} and {100}. This means that the basal {001} face is the most stable, since γ_s is supposed to be proportional to the slice energy of the crystal. This

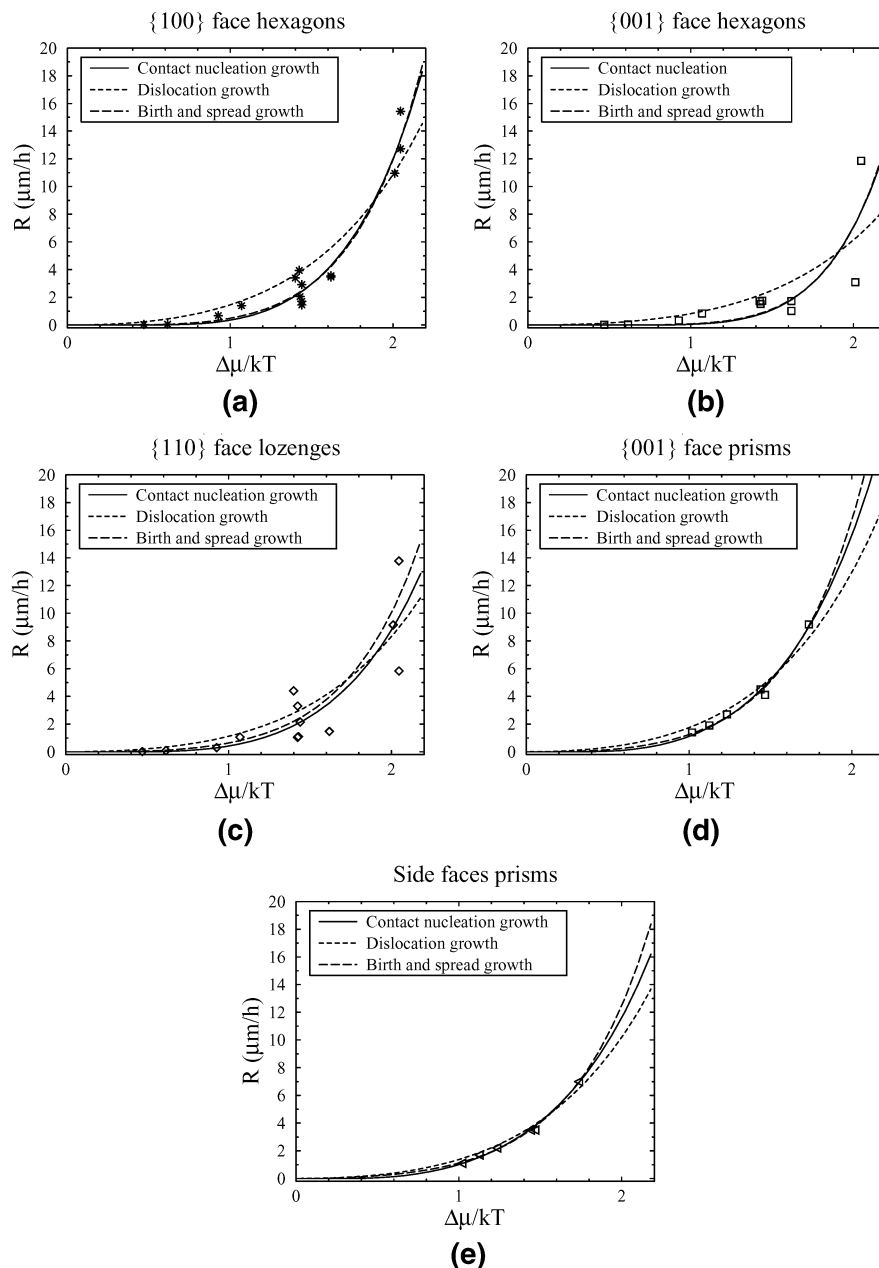


Figure 8. Curve fitting for (a) the $\{100\}$ and (b) the $\{001\}$ faces of hexagons, (c) the $\{110\}$ faces of lozenges, and (d) the $\{001\}$ and (e) the side faces of prisms. In all cases, $C = 200$ g/L Na_2CO_3 and $T = 80$ °C. The best fits are contact nucleation growth at linear step edges and birth and spread growth mechanism. For the curve fitting of prismatic gibbsite crystals ((d) and (e)), the data of King⁴ are used.

agrees with the relative morphological importance of gibbsite faces found earlier by experiment^{10,11} and by a connected net analysis.²⁷ Since the surface energies estimated from the two different 2D nucleation mechanisms are both realistic, no conclusion can be drawn, which one controls gibbsite growth. One might argue that for increasing caustic concentrations, where more 3D nuclei are formed, some of which may be on the surfaces of other crystals, it is more likely that contact nucleation becomes the dominant growth mechanism.

Conclusions

In this study, in-situ optical microscopy was used to measure the growth rate of individual crystal faces, i.e., $\{001\}$, $\{110\}$, and $\{100\}$, of different types of gibbsite

crystal. A significant growth rate dispersion was observed for similar $\{hkl\}$ faces of crystals of the same type within one experiment, in time and between experiments, despite the fact that they were grown under the same external conditions.

To determine the dependence of the average growth rate of the different forms $\{hkl\}$ of crystals of the same type on the driving force, we have derived a definition of the driving force adapted for gibbsite crystallization from caustic aluminate solution. Furthermore, besides the well-known crystal growth models for birth and spread and spiral growth, a new analytical model for contact nucleation is introduced.

Fits of the growth rates observed using the analytical expressions for birth and spread, spiral growth, and contact nucleation revealed that for all different faces,

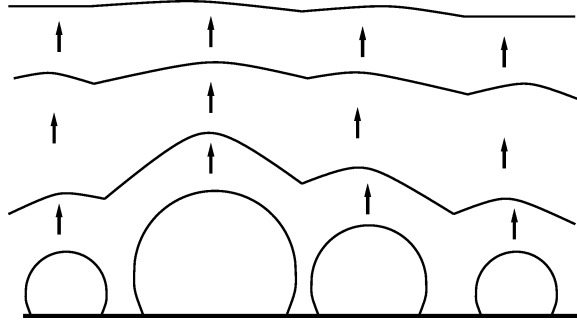


Figure 9. Step generation by 2D contact nucleation from a linear edge.

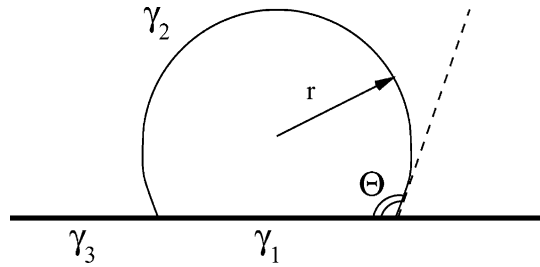


Figure 10. 2D nucleus in contact with a linear edge on a crystal surface. The symbols γ_1 , γ_2 , and γ_3 are the edge free energies of a the nucleus-edge, nucleus-mother phase, and edge-mother phase boundary, respectively.

birth and spread, and contact nucleation are the most probable growth mechanisms. This is in accordance with earlier surface topography studies.

From the fitted data, the edge free energies have been determined. They are consistent with the morphological importance of the several faces, i.e., $MI_{001} > MI_{\text{sidefaces}}$ as has been observed^{10,11} and calculated.²⁷

Acknowledgment. Billiton Aluminium B.V. is kindly acknowledged for the financial support and permission to publish this work. Further, the authors are grateful to Prof. E. Vlieg for stimulating this investigation.

Appendix

In this appendix, we derive an expression for the growth of a crystal face, for which the steps are generated by multiple 2D contact nucleation at the intersection line of a foreign body with the crystal surface. The essentials of the model are shown in Figure 9. It is assumed that individual nuclei are constantly formed along the contact line because of a lowering of the 2D nucleation barrier. These nuclei coalesce to steps that propagate away from this linear edge. We first derive the frequency of 2D nucleation per edge site, followed by calculation of the rate of step creation using a one-dimensional version of the birth and spread nucleation model.

Consider a 2D circular nucleus contacting a linear edge with an angle θ , as is shown in Figure 10. The total free energy for creating this nucleus equals

$$\Delta G_{\text{tot}} = \Delta G_{\text{surface}} + \Delta G_{\text{edge}} \quad (18)$$

or

$$\Delta G_{\text{tot}}(r) = -\frac{\Delta\mu}{\Omega^{2/3}} r^2 C_A + r C_B \quad (19)$$

with $C_A = (\theta - 1/2 \sin 2\theta)$ and $C_B = 2\gamma_2\theta + 2(\gamma_1 - \gamma_3) \sin(\pi - \theta)$. In this equation, γ_1 , γ_2 , and γ_3 are the edge free energies of the boundaries between nucleus-edge, nucleus-mother phase, and edge-mother phase, respectively. $\Delta\mu$ is the driving force for growth and Ω is the volume of a growth unit. Using Young's equation (see also Figure 10)

$$\gamma_3 = \gamma_1 + \gamma_2 \cos \theta \quad (20)$$

C_B becomes equal to $2\gamma_2(\theta - 1/2 \sin 2\theta)$, or $C_B = 2C_A\gamma_2$. Now eq 19 becomes

$$\Delta G_{\text{tot}}(r) = C_A \left(-\frac{\Delta\mu}{\Omega^{2/3}} r^2 + 2\gamma_2 r \right) \quad (21)$$

Differentiating $\Delta G_{\text{tot}}(r)$ with respect to r and putting this equal to zero gives the radius for 2D nucleation

$$r^* = \frac{\gamma_2 \Omega^{2/3}}{\Delta\mu} \quad (22)$$

which is identical to the critical radius for homogeneous nucleation. Subsequently, the barrier for 2D nucleation, which corresponds to the maximum value of $\Delta G_{\text{tot}}(r)$, can be evaluated as

$$\Delta G^* = \frac{\gamma_2^2 \Omega^{2/3}}{\Delta\mu} \left(\theta - \frac{1}{2} \sin 2\theta \right) \quad (23)$$

Now, we assume that a 2D nucleus only expands if its radius exceeds the critical nucleus r^* . Using Boltzmann statistics,²⁸ it follows that the concentration of critical nuclei along the linear edge is given by

$$c_{r^*} = c_{\text{eq}} \exp\left(\frac{\Delta\mu}{kT}\right) \exp\left(\frac{-\Delta G^*}{kT}\right) \quad (24)$$

where c_{eq} is the equilibrium concentration of the solute in the liquid. If one growth unit is added to a critical nucleus, it is assumed to become supercritical and will expand. From this, it follows that the rate of nucleation per site along the linear edge equals

$$I = v_c c_{r^*} \quad (25)$$

Here, v_c is the probability of adding a growth unit to an existing critical nucleus. The probability is given by the product of the concentration of growth units in the liquid, $c_{\text{eq}} \exp(\Delta\mu/kT)$, their probability of entering to the step of the nucleus, $(kT/h) \exp(-\Delta G^\ddagger/kT)$, and the circumference of the nucleus, excluding the contact line with the linear edge, $2\theta r^*$. ΔG^\ddagger is the activation free energy for incorporation at the step. This leads to

$$v_c = C_C \exp\left(\frac{\Delta\mu}{kT}\right) (\Delta\mu)^{-1} \quad (26)$$

with $C_C = 2\theta\gamma_2\Omega^{2/3}c_{\text{eq}}(kT/h) \exp(-\Delta G^\ddagger/kT)$. Combining eq 24, 25, and 26 gives the rate of nucleation

$$I = C_C c_{\text{eq}} \left(\exp\left(\frac{2\Delta\mu}{kT}\right) (\Delta\mu)^{-1} \exp\left(\frac{-\Delta G^*}{kT}\right) \right) \quad (27)$$

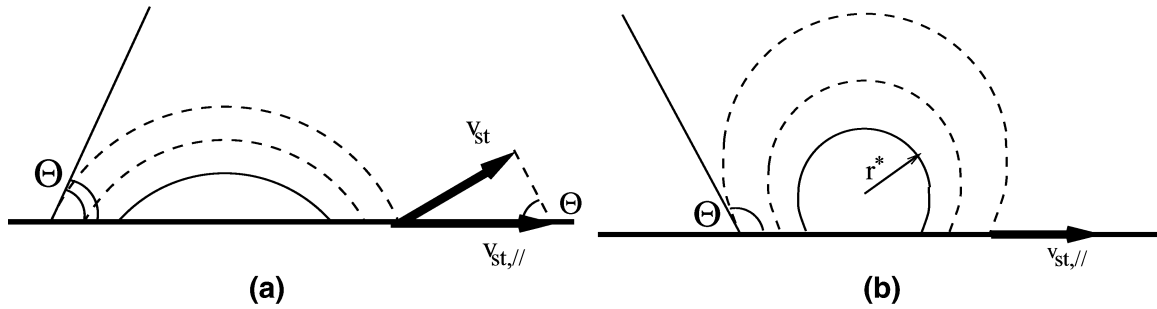


Figure 11. Step movement from a supercritical nucleus along a linear edge; (a) $\theta < 90^\circ$: $v_{st,||} = v_{st}/(\sin \theta)$, (b) $\theta > 90^\circ$: $v_{st,||} \approx v_{st}$.

Using the 2D nucleation frequency per step site as derived above, we now calculate the rate of step generation using a one-dimensional version of the birth and spread model. The length of coverage of the linear edge by a 2D nucleus formed at time t_1 is at time t_2 equal to

$$L(t_2 - t_1) = 2v_{st,||}(t_2 - t_1) \quad (28)$$

with $v_{st,||} = g(\theta)v_{st}$, the step velocity parallel to the linear edge. The geometrical factor, $g(\theta)$, depends on the contact angle θ . As shown in Figure 11a, for $\theta < 90^\circ$ $v_{st,||} = v_{st}/(\sin \theta)$, i.e., $g(\theta) = 1/(\sin \theta)$. For $\theta > 90^\circ$, the situation is more complex, but as shown in Figure 11b, $g(\theta)$ can be approximated to 1. If there are N positions along the linear edge, a new, complete step is generated at time τ , which satisfies

$$\int_0^\tau NIL(\tau - t)dt = N \quad (29)$$

Here, NI is the formation frequency of critical nuclei on the total length of the linear edge. Combining eq 28 with 29 and solving the integral, one obtains

$$\tau = (IV_{st,||})^{-1/2} \quad (30)$$

The growth rate, R_d , induced by contact nucleation is the product of the frequency of step generation, τ^{-1} , times the step height, h_{st} , or

$$R_c = h_{st}(IV_{st,||})^{1/2} \quad (31)$$

with $v_{st,||} = v_0(\exp(\Delta\mu/kT) - 1)g(\theta)$. Finally, combining eqs 23, 27, and 31 an explicit expression for the growth rate induced by contact nucleation is obtained

$$R_c = h_{st} \left(C_C c_{eq} \exp\left(\frac{2\Delta\mu}{kT}\right) (\Delta\mu)^{-1} \times \exp\left(\frac{-\Delta G^*}{2kT}\right) \right)^{1/2} \left(v_0 \left(\exp\left(\frac{\Delta\mu}{kT}\right) - 1 \right) g(\theta) \right)^{1/2} \quad (32)$$

or more compact

$$R_c = C_1 \left(\exp\left(\frac{\Delta\mu}{kT}\right) - 1 \right)^{1/2} \exp\left(\frac{\Delta\mu}{kT}\right) (\Delta\mu)^{-1/2} \exp\left(\frac{-C_2}{\Delta\mu}\right) \quad (33)$$

with C_1 and C_2 constants, independent of the driving force, equal to $C_1 = h_{st}c_{eq} (2\theta\gamma_2\Omega^{2/3}v_0g(\theta)(kT/h)$

$\exp(-\Delta G^*/kT))^{1/2}$, and $C_2 = \gamma_s^2\Omega^{2/3}/2kT(\theta - 1/2 \sin(2\theta))$. If the edge free energy is expressed as J/m^2 instead of J/m , then C_2 becomes $C_2 = \gamma_s^2\Omega^{4/3}/2kT(\theta - 1/2 \sin(2\theta))$.

References

- (1) Nielsen, A. E. *J. Cryst. Growth* **1984**, *67*, 289–310.
- (2) Pearson, T. G. *The Chemical Background of the Aluminium Industry*; Royal Institute of Chemistry: London, 1955; Monograph no. 3.
- (3) Misra, C.; White, E. T. *Chem. Eng. Prog. Symp. Ser.* **1971**, *67*, 53.
- (4) King, W. R. *Light Met.* **1973**, 551.
- (5) Halfon, A.; Kaliaguine, S. *Can. J. Chem. Eng.* **1976**, *54*, 160.
- (6) White, E. T.; Bateman, S. H. *Light Met.* **1988**, 157.
- (7) Söhnel, O.; Garside, J.; Eds. *Precipitation*; Butterworth-Heinemann: Oxford, 1992.
- (8) Nielsen, A. E. In *Industrial Crystallization*; Jancic, S. J., Grootcholten, P. A. M., Eds.; Delft University Press: The Netherlands, 1984; pp 35–52.
- (9) Lee, M.-Y.; Parkinson, G. *J. Cryst. Growth* **1999**, *198/199*, 270–274.
- (10) Sweegers, C.; Meekes, H.; van Enckevort, W. J. P.; Ben-nema, P.; Hiralal, I. D. K.; Rijkeboer, A. *J. Cryst. Growth* **1999**, *197*, 244–253.
- (11) Sweegers, C.; Plomp, M.; de Coninck, H. C.; Meekes, H.; van Enckevort, W. J. P.; Hiralal, I. D. K.; Rijkeboer, A. *Appl. Surf. Sci.* **2002**, *187*, 218–234.
- (12) Veessler, S.; Boistelle, R. *J. Cryst. Growth* **1993**, *130*, 411–415.
- (13) Veessler, S.; Boistelle, R. *J. Cryst. Growth* **1994**, *142*, 177–183.
- (14) Zambo, J. *Light Met.* **1986**, 199.
- (15) Sipos, P.; Capewell, S. G.; May, P. M.; Hefter, G.; Laurency, G.; Lukacs, F.; Roulet, R. *J. Chem. Soc., Dalton Trans.* **1998**, 3007–3012.
- (16) Vernon, C.; Parkinson, G.; Lau, D. *Proc. of the Fifth International Alumina Quality Workshop*, 1999.
- (17) Radnai, T.; Hefter, G. T.; Sipos, P. *J. Phys. Chem.* **1998**, *102*, 7841–7850.
- (18) Tossell, J. A. *Am. Mineral.* **1999**, *84*, 1641–1649.
- (19) Veessler, S.; Roure, S.; Boistelle, R. *J. Cryst. Growth* **1994**, *135*, 505–512.
- (20) McCoy, B. N.; Dewey, J. L. *Light Met.* **1982**, 173.
- (21) Smith, P.; Woods, G. *Light Met.* **1993**, 113.
- (22) Cornell, J. B.; Pannett, D. S.; Sullivan, N. S.; Clarke, P. C.; Bailey, C. M. *Proc. of the Fifth International Alumina Quality Workshop*, Bunbury, **1999**, *1*, 153–161.
- (23) Brown, N. *J. Cryst. Growth* **1972**, *12*, 39–45.
- (24) Rossiter, D. S.; Fawell, P. D.; Ilievski, D.; Parkinson, G. M. *J. Cryst. Growth* **1998**, *191*, 525–536.
- (25) Burton, W. K.; Cabrera, N. *J. Phys. U.S.S.R.* **1945**, *9*, 392.
- (26) Farhadi, F.; Babaheidary, M. B. *J. Cryst. Growth* **2002**, *234*, 721–730.
- (27) Sweegers, C.; Boerrigter, S. X. M.; Grimbergen, R. F. P.; Meekes, H.; Fleming, S.; Hiralal, I. D. K.; Rijkeboer, A. *J. Phys. Chem. B* **2002**, *106*, 1004–1012.
- (28) Liu, X. Y.; Maiwa, K.; Tsukamoto, K. *J. Chem. Phys.* **1997**, *106*, 1870–1879.